

Universiteit
Leiden
The Netherlands

Forces and symmetries in cells and tissues

Eckert, J.

Citation
Eckert, J. (2022, December 6). *Forces and symmetries in cells and tissues*. *Casimir PhD Series*. Retrieved from https://hdl.handle.net/1887/3492626

Version:	Publisher's Version
License:	Licence agreement concerning inclusion of doctoral thesis in the Institutional Repository of the University of Leiden
Downloaded from:	https://hdl.handle.net/1887/3492626

Note: To cite this publication please use the final published version (if applicable).

Chapter 3

Cell-Cell Separation Device: measurement of intercellular detachment forces

Whether at the intermolecular or cellular level in organisms, cell-cell adhesion adapts to external mechanical cues arising from the static environment of cells and from dynamic interactions between neighboring cells. Cell-cell adhesions need to resist to detachment forces to secure the integrity and internal organization of organisms. In the past decades, various techniques have been developed to characterize adhesion properties of molecules and cells *in vitro*, and to understand how they sense and probe their environment. Atomic force microscopy and dual pipette aspiration, where cells are mainly present in suspension, are common applications for studying detachment forces of cell-cell adhesions. How cell-cell adhesion forces are developed for adherent and environment-adapted cells is unclear. Here, we designed the Cell-Cell Separation Device (CC-SD), a substrate that measures both intercellular forces and external stresses of cells towards the matrix. The design is based on micropillar arrays for cell traction force measurements. We produced PDMS micropillar-blocks, on which cells adhered to and connected over the spacing. Controlled stretching changed the distance between the blocks and the applied strain at the cell-cell contact, resulting in cell-cell adhesion detachment, which was measured by pillar deflections. Our first experiments gave an insight into technical challenges to measure dynamic changes of cell-cell adhesions under stress. The CC-SD provided an increase of the gap between the blocks of up to 140%, which was sufficient to separate substrate-attached cells with fully developed F-actin network. Simultaneously measured pillar deflections resulted in cellular responds to the intercellular strain. Our novel CC-SD opens up possibilities for the analysis of intercellular force detachments and sheds light on the robustness of cell-cell adhesions in dynamic processes in tissue development.

This chapter is based on: **Eckert, J.**, Partel, S., Matylitskaya, V. , Kasemann, S., and Schmidt, T. Cell-Cell Separation Device – measurement of intercellular detachment forces. *In preparation.*

3.1 Introduction

Cells are dynamically in contact with each other and with the extracellular matrix (ECM). They experience external mechanical forces applied by neighboring cells and sense, individually or together, changes of the cellular environment, e.g. topography (*1*) and stiffness (*2*). The physical and passive interactions are converted into biochemical signals, which cause an active response followed by an alteration of cell-cell adhesion (*3*, *4*). These complex cell-cell adhesions have to resist detachment forces (*5*). Various techniques have been developed to characterize the properties of cells *in vitro* and to understand how they sense and probe their environment. These techniques and their further development for studying cell-cell adhesions have been described in detail in recent reviews (*6–13*). In most methodical approaches, like atomic force microscopy (*14*, *15*) and dual pipette aspiration (*16*, *17*), the detachment forces of cells were studied in a suspended form to avoid cell-ECM interactions. In the experiments, cells were brought into contact for a short period of time without developing an actin stress fiber network. Using other techniques such as Förster resonance energy transfer (FRET)-based tension sensors, traction force microscopy (TFM), and the micropillar array technology deal with spread cells on substrates and give an insight into the force and tension interactions of cells (*18–23*). The intercellular forces are predicted to be dependent on the ECM-property-dependent traction forces, cell spreading area and shape, cell-cell contact size, and on the cell type with its different cell-cell adhesion machinery. All these measurements were carried out in dynamical equilibrium and did not give information about detachment forces.

Here, we combined the ideas of measuring intercellular detachment forces of cells in the spread state with developed actin stress fibers by our novel device. Our Cell-Cell Separation Device (CC-SD) was able to obtain intercellular forces through traction force measurements of deflected micropillars. For this, the pillars were connected to PDMS-blocks on which cells adhered to and were allowed to connect across the gap. An applied stretch on a thin substrate underneath the blocks increased the distance between the cells until the cell-cell contact broke. Our first experiments gave an insight into technical challenges to measure dynamic changes of cell-cell adhesions under external stress. We demonstrated that our CC-SD provided a nominal strain at the cell-cell contact by an increase of the gap width between the blocks by up to 140%, i.e. 2.4-fold, which was sufficient to separate substrate-attached cells with fully developed actin stress fiber network. Simultaneously, pillar deflections caused by cell traction forces

gave information about the cellular responses to the intercellular strain. Our novel designed CC-SD opens up possibilities for the analysis of intercellular force detachments and sheds light on the robustness of cell-cell adhesions in dynamic processes in tissue development.

3.2 Results

3.2.1 The intercellular adhesion strength increases with an increase of the total traction force

Cells form doublets (Fig.3.1A) or larger clusters up to confluent monolayers, ultimately forming tissues that define the organism. The stability of such assembly is secured by the interplay of cell-matrix to cell-cell adhesions (*4*). At the single-cell level, where solely cell-matrix adhesion is important, it has been shown that the summed absolute traction force that individual 3T3 fibroblast cells exert on the extracellular matrix scales with the cell spreading area. Likewise, for cells on fibronectin-coated micropillars the total absolute traction force was found to increase proportional to the number of deflected pillars below the cell (*24*, *25*). The question we asked here was, whether this linear scaling between interaction area and total absolute force prevails for cell assemblies, i.e. here for cell-doublets. In order to test the hypothesis, we cultured cells on flexible micropillars and analyzed the traction forces developed by the cell. Experiments were performed on 46 cell-doublets (Fig.3.1B-C). The total absolute traction force linearly increased with the number of deflected pillars for both the cell doublets and the 92 individual cells after forces were split and assigned to each cell. This relationship was identical for the doublet configuration as well as for individual cells (Fig.3.1D). The resulting mean absolute force per deflected pillar was calculated to be 11.0 ± 2.7 nN for doublets, and 10.9 ± 3.4 nN (mean ± s.d.) for individual cells of 3T3 fibroblasts on fibronectin-coated pillars. Similar results have previously been obtained for single 3T3 fibroblasts ((*25*); Chapter 2).

The above measurements further allowed us to measure the forces that developed at cell-cell contacts (*19*). After partitioning the cell doublet into the two individual cells, we calculated the resultant force, F_c, for each cell, $c1$ and $c2$, summing up the individual traction forces, F_t (Fig.3.1E; Eqs.(3.7)). The resulting forces F_{c1} and F_{c2} were opposing, as required from Newton's law. Our results showed that the intercellular force (Eq.(3.8)) increased with the magnitude of the total traction force exerted by the doublet (Fig.3.1F). About 25% of the total traction force was accounted by the force between the cells. Therefore, we speculate that 25% of the active

adhesion molecules are located at the cell-cell interface.

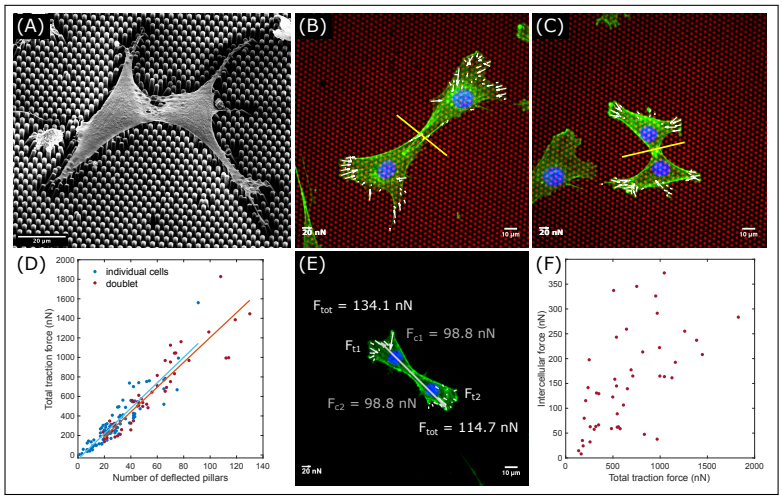


Figure 3.1: The intercellular force increases with the total traction force. *(**A**), Scanning electron microscopy image of a 3T3 fibroblast cell doublet. (**B,C**), Two 3T3 cells connected to a cell-doublet exert traction forces (white arrows) on elastic micropillars. For the traction force analysis of each individual cell, the doublet was separated at the cell-cell contact (yellow line). Red: fibronectin-coated micropillars, green: F-actin, blue: nuclei. (**D**), Total traction force, F_{tot}, per doublet and each individual cell versus the number of deflected pillars. (**E**), Traction forces, F_t of each individual cell add up and result in the intercellular force contribution, F_c. (**F**), The intercellular force, $F_{cc} = |F_{c1}| + |F_{c2}|$, versus the total traction force per doublet. Correlation coefficient: $r = 0.6$.*

3.2.2 Stretching a homogeneous elastic micropillar field causes deformations

In an organism, the static picture we analyzed in the previous subsection is invalid. The forces between cells and the extracellular matrix constantly change due to their activity, hence cell-cell adhesion needs to adapt in a dynamic way to keep tissue integrity. To test how cell-doublets and their individual cells adapt to dynamic mechanical challenges, we designed an experiment that included a dynamical stretch of the elastic micropillar array. Earlier it has been shown that the cell's cytoskeleton largely rearranged on a continued uniaxial stretch (*26*). Here, we used a similar approach to assess whether a uniaxial stretch would lead to a change in cell-cell adhesion forces, and whether we would be able to determine the forces that are sufficient to break a cell-cell contact. We cultured human melanoma MV3 cells on micropillar arrays and mounted arrays of thickness of ∼100 µm with

two clamps in a linear stretcher on our microscope. The clamp-positions were electronically controlled (Fig.3.2A). We first characterize the resulting strain-fields for such homogeneous pillar arrays by analyzing the pillar positions with respect to the external strain applied. At 0% strain, i.e. in an unstretched position, the mean pillar-to-pillar distances was 3.87 ± 0.18 µm (mean ± s.d.) (Fig.3.2B,D). When we applied the stretch in x-direction on the micropillar array, we identified a displacement of the pillars in both the x- and y-directions (Fig.3.2B-C). At 20% nominal strain, the pillar-to-pillar distance increased to 4.05 ± 0.15 µm, i.e. 4.6% in the stretch direction, and decreased to 3.79 ± 0.09 µm (mean ± s.d.), i.e. -2.3% perpendicular to it (Fig.3.2D). The difference is predicted for an incompressible material like PDMS, for which the Poisson ratio $\nu = 0.5$, and hence the strain relation (Eq.(3.6)) holds.

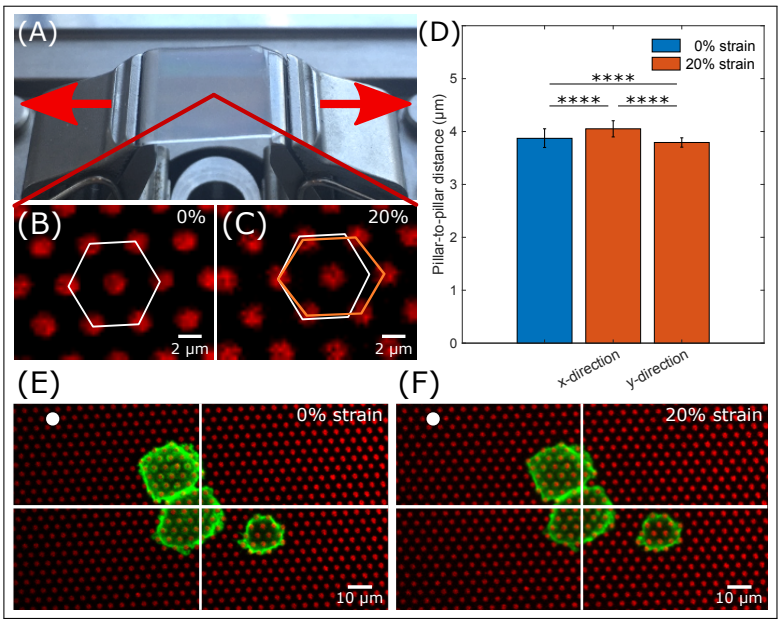


Figure 3.2: x-y displacement changes by less than 5%. *(**A**), A 1x1 cm micropillar array mounted with two clamps. The horizontal stretch direction of the array is indicated by red arrows. (**B**), Top view of micropillars with hexagonal geometry in the unstretched position. (**C**), A strain of 20% on the pillar array caused a deformation of the substrate and thus an increase and decrease of the center-to-center distance in the x- and y-position, respectively, which is indicated by the orange hexagon. Scale bar: 2 µm. (**D**), Pillar-to-pillar distances at 0% and 20% substrate strain in x-direction (n=40). (**E,F**), MV3 cells adhered to micropillars undergo substrate stretching and maintain stable cell-cell adhesions. The white dot represents the reference point of both images. Red: fibronectin-coated micropillars, green: F-actin. Two-sided Wilcoxon rank sum test: **** $p < 0.0001$.*

It is essential for the methodology of force measurements in micropillar assays that the positions of the undeflected pillars are known to high accuracy (*27*). When stretching the substrate, this accuracy might be deteriorated by, for example, pillar deformations and imperfections in the homogeneity of the PDMS polymer. Thus, we further characterized the background deflection field, i.e. excluding pillars covered by cells, of the micropillars on uniaxial stretch. For an unstretched array, the mean deflection was 0.038 ± 0.021 μm (mean ± s.d.) (Fig.S3.7A). This accuracy was predicted from the total signal detected for each pillar on the CCD-detector of the microscope (*27*). At 20 % nominal substrate strain, the mean background deflection increased by 38% to 0.061 ± 0.033 μm (mean ± s.d.) (Fig.S3.7B-C).

To check whether the applied substrate strain affected the traction force of cells, we focused on the pillar deflection analysis of single MV3 cell. These results need to be known in order to rule out the mechanical influence of substrate deformation on the intercellular force calculation. At 0% nominal strain, the mean deflection of the pillars was 0.32 ± 0.17 μm (mean ± s.d.) and thus an order of magnitude higher than the background deflections (Fig.S3.7D). When the 20% nominal strain was applied, the mean deflection of 0.34 ± 0.26 μm (mean ± s.d.) did not change compared to the unstretched position (Fig.S3.7E-F). The stretch of the micropillar and thus the deformation of the pillar field underneath the cell did not affect the mean traction forces of the MV3 cell.

These experiments demonstrated that the micropillar technology can be used to apply a defined stress/strain on both cells and cell assemblies, with the ability to simultaneously monitor the cellular force-response as monitored by the micropillar deflections. Yet, likewise, the results showed a severe limitation of this initial approach: the local strain field, reflected by the pillar-to-pillar displacement, that could be achieved was less than 5% on a nominal substrate stretch of 20%. Probably most of the strain was localized to areas of the substrate weakened by the clamps of the stretcher. The amount of strain that was realized on cells was not sufficient to challenge a cellular response, or even break the cell-cell contacts as shown for the MV3 cells in Fig.3.2E-F.

3.2.3 CC-SD: the Cell-Cell Separation Device

In order to break the cell-cell contact and simultaneously measure the maximum intercellular adhesion force between two cells adhered to substrates in a doublet configuration, we designed a substrate, the Cell-Cell Separation Device (CC-SD) (Fig.3.3A). The substrate is composed of PDMS blocks of

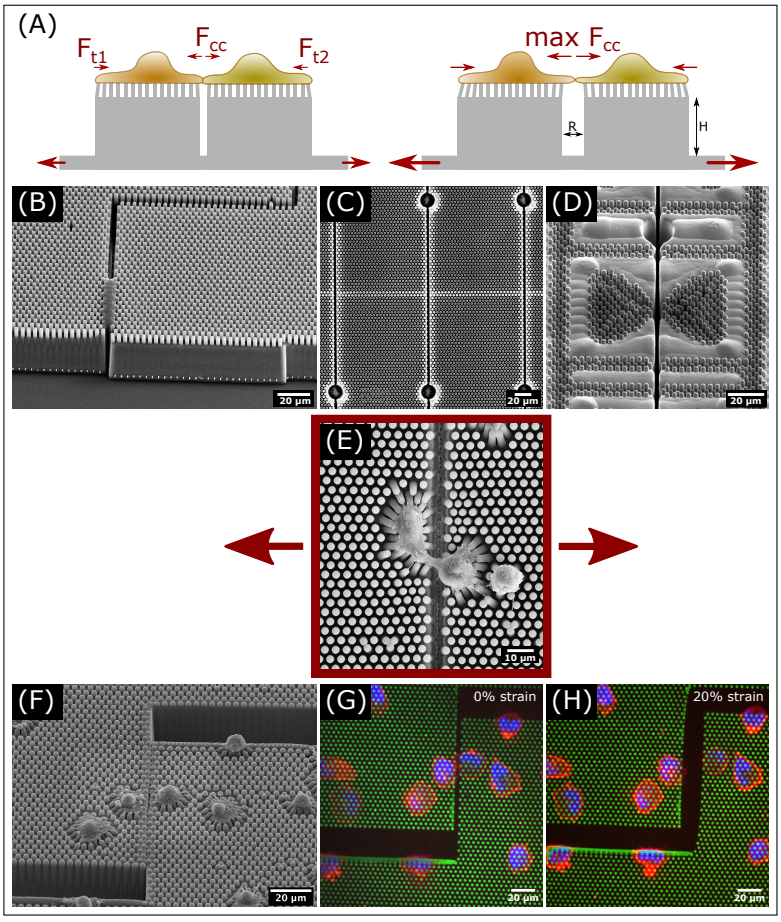


Figure 3.3: Cell-Cell Separation Device (CC-SD). *(**A**), Schematic overview of the CC-SD. Two cells adhered on blocks of height, H, composed of micropillars and connect across a gap of width, R. Obtained traction forces, F_t, (Eqs.(3.7)) result in the intercellular forces, F_{cc} (Eq.(3.8)). By applying a stretch on the connected substrate, the gap width increases, resulting in an increase in pillar deflections, i.e. increase in pseudo-traction forces. At a certain strain, the cell-cell adhesions break and the maximum intercellular force can be obtained. (**B**), CC-SD in a zig-zag configuration for tensile and shear force measurements at the cell-cell contact. (**C**), Parallel gaps perpendicular to the stretch direction. (**D**), CC-SD with pillar fields in a butterfly configuration. The geometry of the wings controls the cell spreading area and contact length between the cells. (**E**), Two MV3 cells adhere across the gap. (**F-H**), CC-SD in a zig-zag configuration. An application of 20% strain is sufficient enough to break the cell-cell contact of MV3 cells. Green: fibronectin-coated micropillars, red: F-actin, blue: nuclei.*

height, H, connected by a thin layer of PDMS at the bottom. On top of each block, a field of micropillars is located to which cells can adhere. The

blocks are spaced in such a way that cells are allowed to connect across the gap of width, R (Fig.3.3E). An externally applied stretch on the thin layer localizes the strain to the gap and increases significantly the block distance, R. This eventually breaks the cell-cell contact.

Our novel design, although adding substantial challenges in the microfabrication process by deep reactive-ion etching (see materials and methods), allowed us to develop additional application modes, which make the CC-SD a versatile instrument. We developed and characterized four CC-SDs in different configurations (Fig.3.3B-D,F) whose specifications are summarized in Tab.S3.1. In one design, the gap was arranged perpendicular to the direction of stretching. That design allowed to apply tensile stress at the cell-cell contact during uniaxial stretching (Fig.3.3C). In a second and third design, the gap was arranged in a zig-zag pattern, allowing additional measurements of shear forces where the blocks separated parallel to the cell-cell contact length (Fig.3.3B). The pillars in the fourth design, inspired by (*19*), were arranged in a butterfly shape to adjust the cell spreading area and allowed the cell-cell contact length to be fixed (Fig.3.3D).

All CC-SDs were designed to be optimized for the cell lines we use in ongoing studies: the 3T3 fibroblast cell line and the MV3 melanoma cell line. As in the design of the homogeneous arrays we used earlier, the micropillar fields on top of the blocks consisted of pillars of ∼2 μm diameter arranged in regular hexagonal patterns of ∼4 μm center-to-center distance. The pillar height was adjusted to the range of suitable effective Young's moduli relevant to the two cell types. For a pillar height of 6.1 μm of the previously used micropillar array (effective Young's modulus: 29.5 kPa), 3T3 fibroblasts and MV3 cells were reported to apply a mean force per pillar of 12.6 ± 5.2 nN ((*25*); Chapter 2) and 19 ± 6 nN (mean ± s.d.) (Fig.S3.6A), respectively. The initial gap width of all CC-SD substrates was set to 4 μm perpendicular to the direction of stretching, a length scale across which 3T3 and MV3 cells were able to span and adhere to each other (Fig.3.3E; Fig.3.4A). The area of the butterfly pattern was chosen to match the mean spreading area of the two cell lines, which was between 117 ± 61 pillars and 122 ± 85 pillars (mean ± s.d.), respectively (Fig.S3.6B). Accordingly, we chose an area of each butterfly wing of 119 pillars.

We set the block height between 30 μm to 40 μm (Fig.3.3B). This height was sufficient to avoid pre-stretching our substrate while mounting. The strain on the CC-SD was mainly localized and applied in the region between the blocks. When we stretched the tensile CC-SD with the perpendicular gap, we identified a linear increase of the gap width of 0.43 ± 0.06 μm per nominal strain, i.e. from ∼6 μm at 0% stretch to ∼16 μm at 20% nominal

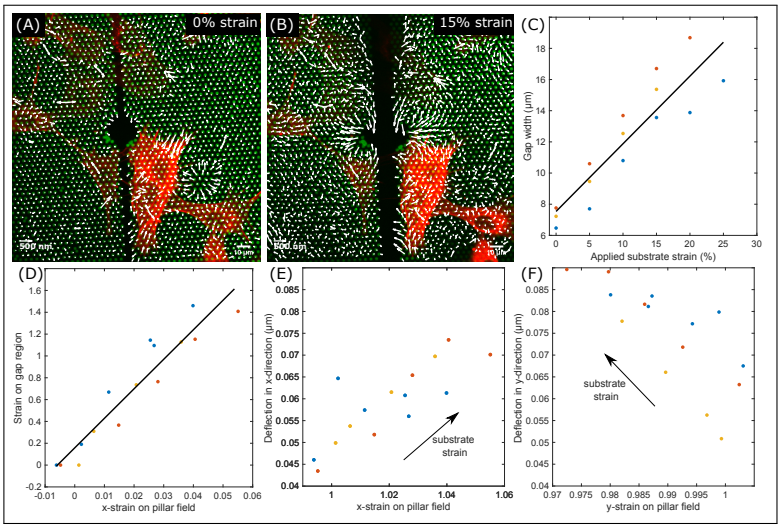


Figure 3.4: Tensile CC-SD. *(**A,B**), CC-SD with the gap perpendicular to the stretch direction, showing 3T3 fibroblasts and the pillar deflection field (white arrows) at 0% and 15% substrate strain. Green: fibronectin-coated micropillars, red: F-actin. (**C**), By applying a strain on the substrate, the width of the gap increases (n = 3). (**D**), The strain on the gap region is 27.04 ± 2.54 bigger than the deformation on the pillar field. (**E,F**), The magnitude of the computed pillar deflections in x- and y-directions increase with increasing substrate strain. The stain on the substrate causes an elongation (increased strain) of the pillar field in x-direction (**E**) and a compression (decreased strain) in y-direction (**F**).*

stretch (Fig.3.4C). Furthermore, we compared the strain in x-direction of the pillar field with the strain on the gap region (Fig.3.4D). The gap width increased by 27.04 ± 2.54 times the pillar-to-pillar distance. In comparison to the tensile stretch of 4.6% of the pillar array (Fig.3.2D-F), the gap width increased by 140.2%, i.e. 2.4-fold.

As shown for the micropillar array above, the substrate deformation caused by the nominal substrate strain affected the accuracy of pillar detections. We showed that the magnitude of the pillar deflections in x- and y-direction increased with increasing substrate strain (Fig.S3.7C). We now wanted to confirm whether the earlier result likewise holds for the CC-SD substrate. For that, we computed the pillar deflections for each nominal substrate strain applied (Fig.3.4E-F). Again, we found an increase of the pillar deflections in x- and y-direction with increasing nominal stretch, which further correlated with the elongation and compression of the substrate, respectively. One example of 3T3 fibroblasts cultured on the tensile CC-SD is shown in Fig.3.5A-B. Two cells adhered to each other across the gap and were stretched by increasing gap width. The mean deflections of

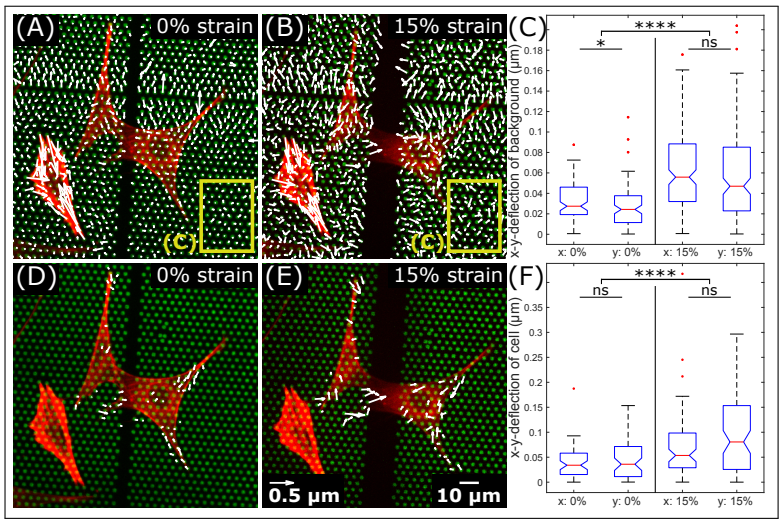


Figure 3.5: Traction forces of cell doublet increases with increasing gap width. *3T3 fibroblast cells cultured on the CC-SD with the gap perpendicular to the direction of stretching. (**A**,**B**), The deflection field of all pillars at 0% and 15% nominal substrate strain. The yellow frame represents the pillars considered for background analysis in (**C**). (**C**), Absolute deflections in x-and y-direction of pillars in a manual selected background region, i.e. excluding pillars covered by cells. In total, 98 and 154 pillars at 0% and 15% nominal strain, respectively, were considered. (**D**,**E**), Deflection of pillars caused by cell traction forces at 0% and 15% nominal substrate strain. All deflections pointing towards the center of the cell are shown and were used for the analysis. (**F**), Absolute deflections in x-and y-direction of pillars deflected by the cell. In total, 58 and 77 pillars at 0% and 15% nominal strain, respectively, were considered. Green: fibronectin-coated pillars, red: F-actin. Two-sided Wilcoxon rank sum test: * $p \leq 0.05$, **** $p < 0.0001$, ^{ns} $p > 0.05$.*

the background were 0.0481 ± 0.0022 µm and 0.0965 ± 0.0039 µm (mean ± s.e.m.) at 0% and 15% nominal strain, respectively (Fig.3.5C). When the stress at the cell-cell contact increased, we expected a cellular response by increasing pillar deflections towards the gap to obey Newton's third law in terms of total force conservation. In order to check whether the strain at the cell-cell contact affected the overall applied traction forces, we analysed the pillar deflections below the cells (Fig.3.5D-E). At 0% strain, the mean deflection caused by the cells was found to be 0.070 ± 0.006 µm (mean ± s.e.m.). When we applied the nominal substrate strain of 15%, the mean pillar deflections increased to 0.137 ± 0.009 µm (mean ± s.e.m.) (Fig.3.5F). Since the mean pillar deflections, $\langle \delta_{\text{all}} \rangle$, below the cells were close to the mean background deflections, $\langle \delta_{\text{bkg}} \rangle$, we needed to correct for the background. Assuming that the real cellular deflections, $\langle \delta_{\text{cell}} \rangle$, are uncorrelated to the background as given by the positional accuracy, the real

mean deflection is given by $\langle\delta_{\text{cell}}\rangle = \sqrt{\langle\delta_{\text{all}}\rangle^2 - \langle\delta_{\text{bkg}}\rangle^2}$ (Eq.(3.4), Eq.(3.5)). This value changed from $\langle\delta_{\text{cell}}\rangle = 0.050 \pm 0.008$ µm at 0% to $\langle\delta_{\text{cell}}\rangle = 0.098 \pm 0.013$ µm at 15% substrate strain. Unfortunately, the pillar height decreased towards the gap due to technical limitations in the manufacturing of the Si-wafer for the PDMS substrate. This challenge needs to be tackled to allow us to translate deflections into forces.

3.3 Discussion and conclusion

Our goal was to provide a design for intercellular force measurements of cells in substrate-attached and spread positions with fully developed actin stress fiber network. The novel design of structured force-sensor fields does allow us now to measure, in real-time, the cellular force response on controlled linear stress at the cell-cell contact of up to 140%, i.e. 2.4-fold. This large increase in gap width was sufficient to successfully break the cell-cell adhesions of MV3 cells (Fig.3.3G-H) and 3T3 fibroblasts (Fig.3.4A-B). Using homogeneous pillar arrays, we saw a deformation of the pillar array when the substrate strain was applied without affecting the mean traction forces of the cells (Fig.S3.7F). For each single cell and cell doublet, the law of conservation of forces must hold. All applied traction forces must sum to zero in mechanical equilibrium. Using the CC-SD by pulling the cells apart from each other and generating a stress at the cell-cell contact, thus we expected a change in the deflection field below the cells as long as they were still in contact (Fig.3.5F). The increased tension at the cell-cell contact would cause an increase in the magnitude of the total pillar deflections per doublet cell, assuming a constant number of deflected pillars for all applied substrate strains. Traction force exertion has been reported to be at least three minutes behind the intercellular signalling process (*28*). Our experiment was performed in a shorter duration of about two minutes. The pillar deflections caused by the cells on our CC-SD substrate were close to the background deflections and were affected by reduced accuracy in pillar detection when a strain was applied. Nevertheless, we recorded a tendency for an increase in the y-direction compared to the x-direction (Fig.3.5F). This led us to speculate whether the cell responded to the increased strain. It has been reported that the applied traction forces of cells act parallel to the cell's elongation ((*25*); Chapter 2). In our presented example, the elongation of both 3T3 fibroblasts is indeed parallel to the gap, i.e. perpendicular to the direction of substrate stretching, and can therefore explain our result. Our novel design will open up possibilities for the analysis of intercellular force detachments in the future and sheds light on the robustness

of cell-cell adhesions in dynamic processes in the development of tissues.

3.4 Materials and methods

Cell culture
3T3 fibroblast and MV3 cells were cultured in high-glucose Dulbecco Modified Eagle's Medium (D6546; Sigma-Aldrich, St. Louis, MO, USA) supplemented with 10% fetal calf serum (Thermo Fisher Scientific, Waltham, MA, USA), 2 mM glutamine, and 100 mg/mL penicillin/streptomycin, 37 °C, 5% CO_2.

Immunostaining
After 22.5 h of spreading, 3T3 fibroblast cells were fixed for 15 min in 4% paraformaldehyde (43368; Alfa Aesar, Haverhill, MA, USA) in phosphate-buffered saline (PBS). Furthermore, cells were permeabilized for 10 min with 0.1% Triton-X 100 in 1% bovine serum albumin (BSA) and blocked for 60 min with 1% BSA in PBS. F-actin was stained with Alexa Fluor 532-labeled phalloidin (A22282; Invitrogen, Carlsbad, CA, USA) and the DNA with DAPI (Sigma-Aldrich).

Life-cell staining
2 h before imaging, F-actin of MV3 cells was stained with CellMask dye (A57245; Invitrogen, DeepRed Actin) and DNA with Hoechst 34580 (63493; Sigma-Aldrich).

Wafer manufacture of CC-SD substrate
The CC-SD substrate was manufactured in several dry etching steps (Fig. S3.8). In a first step, a silicon-wafer of 100 mm in diameter was oxidized by thermal oxidation (SiO_2 thickness: 430 nm). Afterwards, the first photolithography step took place, in which a thin layer of photoresist (PR; MEGAPOSIT SPR 955CM 0.7) was utilized to transfer the desire pattern and open the SiO_2 mask. In this step, the holes that will be the PDMS pillars later were defined. After opening the SiO_2 hard mask, the holes were transferred into the Si-substrate using the Bosch Process or gas chopping process to etch deep into the substrate. The remaining photoresist was removed and another SiO_2 hard mask created by thermal oxidation. Next, the second photoresist layer was applied by spraying. This layer was used to separate the hole arrays (block height, H) followed by opening the oxide mask by deep etching using the Bosch Process. Precise coordination of the etching depth of the two dry etching steps was essential, since this defines

the height of the pillars. This depth is strongly related to the diameter of the holes. In the final step, the remaining silicon oxide was removed by wet chemical etching (BOE).

Elastic micropillar arrays and CC-SD

Polydimethylsiloxane (PDMS, Sylgard 184) micropillar arrays of 2 μm diameter, 6.1 μm (E_{eff} = 29.5 kPa) and 4.1 μm length (E_{eff} = 47.2 kPa), and 4 μm spacing in a hexagonal geometry were used for cell traction force experiments. The pillar arrays were flanked by 50 μm spacers on two sides of the array. Details of this arrangement and the experimental procedures were described earlier in detail (*27*). In brief, pillar arrays were produced on a negative silicon-wafer master made by a two-step deep reactive-ion etching process. Wafers were passivated in trichloro-silane (448931; Sigma-Aldrich). A mixture of 1:10 PDMS (cross-linker/base ratio) was poured onto the Si-master and cured for 20 h at 110 °C. CC-CD substrates were critical point dried. After peeling off, the tops of the pillars were coated by micro-contact printing. For that, flat 1:30 PDMS stamps were incubated for 1 h with 40 mL of 50 mg/mL Alexa Fluor 647–labeled or Alexa Fluor 532–labeled, and 50 mg/mL unlabeled fibronectin (F1141; Sigma-Aldrich), then washed and dried. Subsequently, the stamps were gently loaded onto the ultraviolet-ozone-activated micropillar arrays for 10 min. After stamping, the arrays were passivated with 0.2% Pluronic (F-127, P2443; Sigma-Aldrich) for 1 h, and washed in PBS.

Stretcher

We used an in-house made, piezo-driven stretcher (*26*). PDMS samples of 100 μm thickness were mounted with two clamps (Fig.3.2A). A uniaxial stretch to the PDMS layer was applied by two independent piezo motors (SLC2430s, SmarAct) and a controller unit (MCS-3D, SmarAct, Oldenburg, Germany). An in-house written LabVIEW program was used to control the strain and strain rate. For our experiments, we took images ever 5% strain and increased the strain by a rate of 0.5 %/s.

Microscopy

Samples were imaged at high resolution on a home-build optical microscope setup based on an inverted Axiovert200 microscope body (Carl Zeiss, Oberkochen, Germany), a spinning disk unit (CSU-X1; Yokogawa Electric, Musashino, Tokyo, Japan), and an emCCD camera (iXon 897; Andor Labs, Morrisville, NC, USA). IQ-software (Andor Labs) was used for setup-control and data acquisition. Illumination was performed using fiber-

coupling of different lasers (405 nm (CrystaLaser, Reno, NV, USA), 514 nm (Cobolt AB, Solna, Sweden), and 642 nm (Spectra-Physics Excelsior; Spectra-Physics, Stahnsdorf, Germany)). 3T3 cells on pillar arrays for doublet analysis were placed upside down onto 25 mm cover glasses and inspected with an EC Plan-NEOFLUAR 40× 1.3 Oil Immersion Objective (Carl Zeiss). The stretcher unit for cell-cell separations was mounted on the microscope for inspections.

Scanning electron microscope

After cell fixation and washing steps with PBS buffer, the medium was gradually replaced by a mixture of ethanol and milliQ water: 50%, 70%, 80%, 90%, and 100%. Each incubation step was 10 min. Next, the sample was transferred in 100% ethanol into the chamber of the critical point dryer (CPD 020, Balzers). After the replacement of ethanol with liquid CO_2, the samples were dried. Before the investigation with the scanning electron microscope, samples were coated with lead/platinum.

Pillar stiffness characterization

The traction force to pillar deflection relation was calculated from Euler's theory for flexible beams, supplemented by correction terms (*29*). The total pillar deflection was described by bending, shear, and tilting deflection as

$$\delta = \delta_{\text{bend}} + \delta_{\text{shear}} + \delta_{\text{tilt}}, \tag{3.1a}$$

$$= \left(\frac{16}{3} \left(\frac{h}{d} \right)^3 + \frac{7 + 6\nu}{3} \frac{h}{d} + 8 T_{\text{tilt}} \left(\frac{h}{d} \right)^2 \right) \frac{4}{\pi E d} F_{\text{t}}, \tag{3.1b}$$

where F_{t} is the traction force, E is the Young's modulus, d is the pillar diameter, h is the pillar length, ν is the Poisson ratio, and

$$T_{\text{tilt}} = 1.3 \frac{1 + \nu}{2\pi} \left(2\,(1 - \nu) + \left(1 - \frac{1}{4\,(1 - \nu)} \right) \right). \tag{3.2}$$

is the tilting coefficient (*29*). For our experiment, $\nu = 0.5$ and $E = 2{,}500$ kPa for PDMS. Accordingly, the traction force applied on the pillar was $F_{\text{t}} = k\delta$.

The effective Young's modulus of the pillar field was calculated with (*30*)

$$E_{\text{eff}} = \frac{9k}{2\pi d}. \tag{3.3}$$

Image analysis

Images of MV3 and 3T3 cells within the field of view of 176 × 176 μm were analyzed using MATLAB scripts (MATLAB R2018a; MathWorks, Natick, MA, USA). Pillar deflections were quantified as previously described in detail (*27*). Deflected pillars caused by cell traction forces were distinguished from the background. The background was determined from an undeflected area of the pillar array by selecting a pillar region outside the cell area. Pillar deflections underneath the cell within the background range were excluded.

For cells in the CC-SD images, the mean of cellular deflections was calculated with

$$\langle \delta_{\text{cell}} \rangle = \sqrt{\langle \delta_{\text{all}} \rangle^2 - \langle \delta_{\text{bkg}} \rangle^2}. \tag{3.4}$$

Here, $\langle \delta_{\text{all}} \rangle$ is the mean of all deflections below the cell and $\langle \delta_{\text{bkg}} \rangle$ is the mean deflection of the background. The error of $\langle \delta_{\text{cell}} \rangle$ was derived from the propagation of uncertainty

$$\sigma_{\langle \delta_{\text{cell}} \rangle} = \sqrt{\left(\frac{\partial \langle \delta_{\text{cell}} \rangle}{\partial \langle \delta_{\text{all}} \rangle} s_{\langle \delta_{\text{all}} \rangle} \right)^2 + \left(\frac{\partial \langle \delta_{\text{cell}} \rangle}{\partial \langle \delta_{\text{bkg}} \rangle} s_{\langle \delta_{\text{bkg}} \rangle} \right)^2}, \tag{3.5}$$

with $s_{\langle \delta_{\text{all}} \rangle}$ and $s_{\langle \delta_{\text{bkg}} \rangle}$ the standard error of means.

Poisson correction

To determine the pillar deflections, we considered the x- and y- deformation of the substrate caused by the uniaxial stretch by using the Poisson ratio:

$$\frac{y - y_0}{y_0} = -\nu \frac{x - x_0}{x_0}, \tag{3.6}$$

with x_0, y_0 the unstretched and x, y the stretched positions.

Intercellular force analysis

The intercellular force contribution of each cell in a doublet configuration was calculated with

$$F_{\text{cell},1} = \sum_{i=1}^{N} F_{t1,i}, \tag{3.7a}$$

$$F_{\text{cell},2} = \sum_{i=1}^{M} F_{t2,i}, \tag{3.7b}$$

where F_t is the traction force applied on one of N or M pillars. Considering Eqs.(3.7), the intercellular force results in

$$F_{cc} = |F_{cell,1}| + |F_{cell,2}|. \tag{3.8}$$

Statistics

P-values between two groups were calculated using the two-sided Wilcoxon rank sum test in MATLAB. Data sets were significantly different with probabilities of $p \leq 0.05$ (*); $p < 0.0001$ (****); $p > 0.05$ (ns).

Acknowledgements

J.E. acknowledges Erik Danen (Leiden University) for providing the MV3 cell line.

Author contributions

J.E. conducted and coordinated the research, performed analytic work, experiments, and data analysis. S.K., V.M. and S.P. manufactured the wafer for the CC-SD, J.E. and T.S. wrote the manuscript. T.S. supervised the project.

3.5 Supplementary

Table

		Zig-Zag 1	Zig-Zag 2	Tensile	Butterfly
pillar	height, h (µm)	6.6 to 8.5	1.7 to 2.8	2.5 to 5.4	1.4 to > 10
	diameter, d (µm)	2.3	2.5	2.7	2.5
	stiffness, k (nN/µm)	27.2 to 13.6	866.1 to 308.7	504.1 to 82.5	1235.7 to > 11.8
	E_{eff} (kPa)	16.9 to 8.5	496.3 to 176.9	267.4 to 43.8	708.0 to 6.8
	p-p distance, r (µm)	3.9	3.8	3.7	3.9
	deflection, δ (nm)	108.5	76.1	55.6	–
block	gap width, R (µm)	4.3	x: 4.8, y: 23.1	4.1	3.9
	height, H (µm)	30	35	35	40
	width, W (µm)	110	108	108	128
	length, (µm)	110	108	infinite	infinite

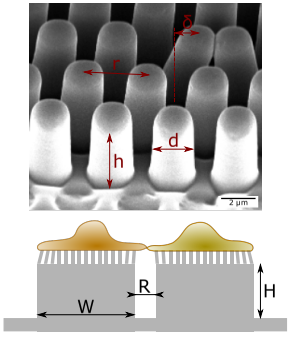


Table S3.1: Cell-Cell Separation Device (CC-SD) specifications. *This table summarizes all characteristics of the four different CC-SDs. The bending stiffness, k, was calculated with* (3.1b) *and the effective Young's modulus, E_{eff} with* (3.3). *All other values were obtained by analyzing SEM images using ImageJ and Matlab software. The substrates are made of PDMS with a Young's modulus of $E = 2500$ kPa.*

Figures

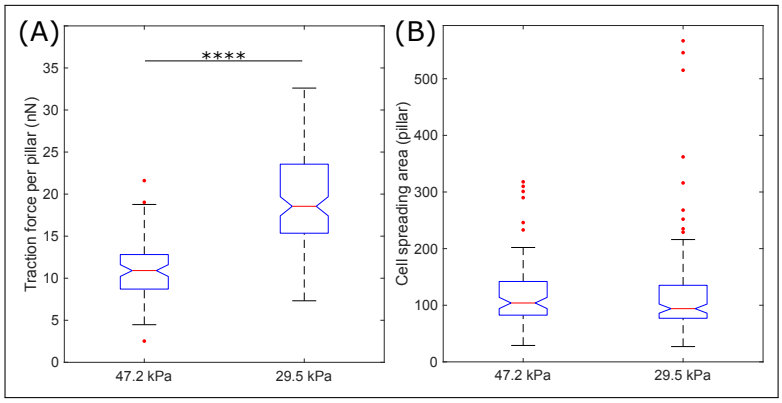


Figure S3.6: *Single MV3 cells cultured on elastic micropillar arrays with Young's modulus of 47.2 kPa and 29.5 kPa (n_{stiff}=85, n_{soft}=128). (**A**), Cells apply larger traction forces on soft pillars compared to stiff. (**B**), The cell spreading areas are equal. Two-sided Wilcoxon rank sum test: **** $p < 0.0001$.*

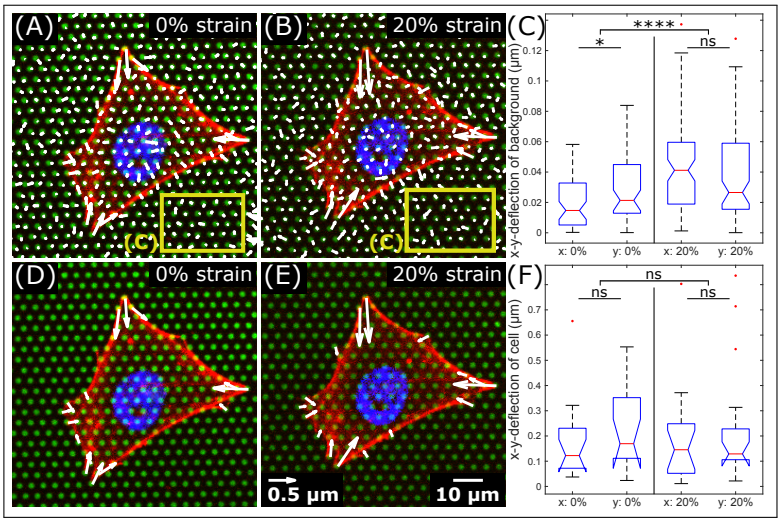


Figure S3.7: *A single MV3 cell cultured on an elastic micropillar array with Young's modulus of 47.2 kPa. (**A**,**B**), The deflection field of all pillars at 0% and 20% nominal substrate strain. The yellow frame represents the pillars considered for background analysis in (**C**). (**C**), Absolute deflections in x-and y-direction of pillars in a manual selected background region, i.e. excluding pillars covered by cells. In total, 54 and 82 pillars at 0% and 20% nominal strain, respectively, were considered. (**D**,**E**), Deflection of pillars caused by cell traction forces at 0% and 20% nominal substrate strain. Only deflections towards the center of mass of the cell are shown. Background forces were excluded. (**F**), Absolute deflections in x-and y-direction of pillars deflected by the cell. In total, 15 and 16 pillars at 0% and 20% nominal strain, respectively, were considered. Green: fibronectin-coated micropillars, red: F-actin, blue: nuclei. Two-sided Wilcoxon rank sum test: * $p \leq 0.05$, **** $p < 0.0001$, ^{ns} $p > 0.05$.*

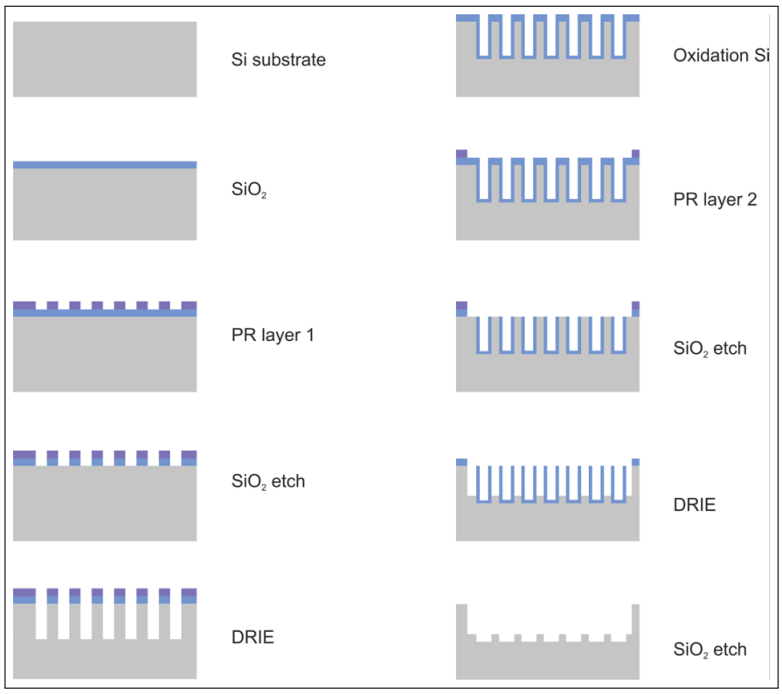


Figure S3.8: *A silicon-wafer is oxidized by thermal oxidation (SiO_2 in blue). Afterwards, the first photolithography step takes place, in which a thin layer of photoresist (PR in purple) is utilized to transfer the desire pattern and open the SiO_2 mask. In this step, the holes that will be the PDMS pillars later are defined. After opening the SiO_2 hard mask, the holes are transferred into the Si-substrate using the Bosch Process or gas chopping process to etch deep into the substrate (DRIE). The remaining photoresist is removed and another SiO_2 hard mask (blue) created by thermal oxidation. Next, the second photoresist layer (purple) is applied by spraying. This layer is used to separate the hole arrays (block height H) followed by opening the oxide mask by deep etching using the Bosch Process. In the final step, the remaining silicon oxide is removed by wet chemical etching (BOE).*

CHAPTER 3

References

(*1*) Lehnert, D., Wehrle-Haller, B., David, C., Weiland, U., Ballestrem, C., Imhof, B. A., and Bastmeyer, M. (2004). Cell behaviour on micropatterned substrata: limits of extracellular matrix geometry for spreading and adhesion. *Journal of Cell Science 117*, 41–52.

(*2*) Reinhart-King, C. A., Dembo, M., and Hammer, D. A. (2008). Cell-cell mechanical communication through compliant substrates. *Biophysical journal 95*, 6044–6051.

(*3*) Yap, A. S., Duszyc, K., and Viasnoff, V. (2018). Mechanosensing and Mechanotransduction at Cell–Cell Junctions. *Cold Spring Harbor Laboratory Press 10*, a028761.

(*4*) Arslan, F. N., Eckert, J., Schmidt, T., and Heisenberg, C.-P. (2021). Holding it together: when cadherin meets cadherin. *Biophysical Journal 120*, 4182–4192.

(*5*) Charras, G., and Yap, A. S. (2018). Tensile Forces and Mechanotransduction at Cell–Cell Junctions. *Current Biology 28*, R445–R457.

(*6*) Kashef, J., and Franz, C. M. (2015). Quantitative methods for analyzing cell–cell adhesion in development. *Developmental Biology 401*, 165–174.

(*7*) Polacheck, W. J., and Chen, C. S. (2016). Measuring cell-generated forces: a guide to the available tools. *Nature Methods 13*, 415–423.

(*8*) Campàs, O. (2016). A toolbox to explore the mechanics of living embryonic tissues. *Seminars in cell & developmental biology 55*, 119–130.

(*9*) Sugimura, K., Lenne, P.-F., and Graner, F. (2016). Measuring forces and stresses in situ in living tissues. *Development 143*, 186–196.

(*10*) Rehfeldt, F., and Schmidt, C. F. (2017). Physical probing of cells. *Journal of Physics D: Applied Physics 50*, 463001.

(*11*) Roca-Cusachs, P., Conte, V., and Trepat, X. (2017). Quantifying forces in cell biology. *Nature Cell Biology 19*, 742–751.

(*12*) Basoli, F., Giannitelli, S. M., Gori, M., Mozetic, P., Bonfanti, A., Trombetta, M., and Rainer, A. (2018). Biomechanical Characterization at the Cell Scale: Present and Prospects. *Frontiers in Physiology 9*, 1449.

(*13*) Gómez-González, M., Latorre, E., Arroyo, M., and Trepat, X. (2020). Measuring mechanical stress in living tissues. *Nature Reviews Physics 2*, 300–317.

(*14*) Benoit, M., Gabriel, D., Gerisch, G., and Gaub, H. E. (2000). Discrete interactions in cell adhesion measured by single-molecule force spectroscopy. *Nature Cell Biology 2*, 313–317.

(*15*) Puech, P.-H., Taubenberger, A., Ulrich, F., Krieg, M., Muller, D. J., and Heisenberg, C.-P. (2005). Measuring cell adhesion forces of primary gastrulating cells from zebrafish using atomic force microscopy. *Journal of Cell Science 118*, 4199–4206.

(*16*) Sung, K., Sung, L., Crimmins, M., Burakoff, S., and Chien, S. (1986). Determination of junction avidity of cytolytic T cell and target cell. *Science 234*, 1405–1408.

(*17*) González-Bermúdez, B., Guinea, G. V., and Plaza, G. R. (2019). Advances in Micropipette Aspiration: Applications in Cell Biomechanics, Models, and Extended Studies. *Biophysical Journal 116*, 587–594.

(*18*) Zhao, B., Li, N., Xie, T., Bagheri, Y., Liang, C., Keshri, P., Sun, Y., and You, M. (2020). Quantifying tensile forces at cell–cell junctions with a DNA-based fluorescent probe. *Chemical Science 11*, 8558–8566.

(*19*) Liu, Z., Tan, J. L., Cohen, D. M., Yang, M. T., Sniadecki, N. J., Ruiz, S. A., Nelson, C. M., and Chen, C. S. (2010). Mechanical tugging force regulates the size of cell-cell junctions. *Proceedings of the National Academy of Sciences of the United States of America 107*, 9944–9949.

(*20*) Maruthamuthu, V., Sabass, B., Schwarz, U. S., and Gardel, M. L. (2011). Cell-ECM traction force modulates endogenous tension at cell–cell contacts. *Proceedings of the National Academy of Sciences 108*, 4708–4713.

(*21*) McCain, M. L., Lee, H., Aratyn-Schaus, Y., Kléber, A. G., and Parker, K. K. (2012). Cooperative coupling of cell-matrix and cell–cell adhesions in cardiac muscle. *Proceedings of the National Academy of Sciences 109*, 9881–9886.

(*22*) Mertz, A. F., Che, Y., Banerjee, S., Goldstein, J. M., Rosowski, K. A., Revilla, S. F., Niessen, C. M., Marchetti, M. C., Dufresne, E. R., and Horsley, V. (2013). Cadherin-based intercellular adhesions organize epithelial cell–matrix traction forces. *Proceedings of the National Academy of Sciences 110*, 842–847.

(*23*) Ng, M. R., Besser, A., Brugge, J. S., and Danuser, G. (2014). Mapping the dynamics of force transduction at cell–cell junctions of epithelial clusters. *eLife 3*, e03282.

(*24*) Eckert, J., van Loon, J. J. A., Eng, L. M., and Schmidt, T. (2021). Hypergravity affects cell traction forces of fibroblasts. *Biophysical Journal 120*, 773–780.

(*25*) Eckert, J., Abouleila, Y., Schmidt, T., and Mashaghi, A. (2021). Single Cell Micro-Pillar-Based Characterization of Endothelial and Fibroblast Cell Mechanics. *Micro 1*, 242–249.

(*26*) Balcioglu, H. E., van Hoorn, H., Donato, D. M., Schmidt, T., and Danen, E. H. J. (2015). The integrin expression profile modulates orientation and dynamics of force transmission at cell–matrix adhesions. *Journal of Cell Science 128*, 1316–1326.

(*27*) van Hoorn, H., Harkes, R., Spiesz, E. M., Storm, C., van Noort, D., Ladoux, B., and Schmidt, T. (2014). The Nanoscale Architecture of Force-Bearing Focal Adhesions. *Nano Letters 14*, 4257–4262.

(*28*) van Hoorn, H., Donato, D. M., Balcioglu, H. E., Danen, E. H., and Schmidt, T. (2018). p130Cas contributes to cellular mechanosensing and force exertion. *bioRxiv*.

(*29*) Schoen, I., Hu, W., Klotzsch, E., and Vogel, V. (2010). Probing Cellular Traction Forces by Micropillar Arrays: Contribution of Substrate Warping to Pillar Deflection. *Nano Letters 10*, 1823–1830.

(*30*) Ghibaudo, M., Saez, A., Trichet, L., Xayaphoummine, A., Browaeys, J., Silberzan, P., Buguin, A., and Ladoux, B. (2008). Traction forces and rigidity sensing regulate cell functions. *Soft Matter 4*, 1836–1843.